5-2021

Classical Simulations of Ultracold Chemical Reactions

Mark Lide
Trinity University, mark.lide99@gmail.com

Classical Simulations of Ultracold Chemical Reactions

by

Mark H. Lide

An honors thesis submitted to the Department of Physics & Astronomy at

TRINITY UNIVERSITY

in partial fulfillment of the requirements for the

Bachelor of Science in Physics

May 2021

Accepted by . . . .
Prof. Kelvin Cheng

Accepted by . . . .
Prof. Nirav Mehta

Accepted by . . . .
Prof. David Pooley

Accepted by . . . .
Prof. Orrin Shindell

Accepted by . . . .
Prof. Jennifer Steele, Chair

Accepted by . . . .
Prof. Niescja Turner

Accepted by . . . .
Prof. Dennis Ugolini

Classical Simulations of Ultracold Chemical Reactions

by

Mark H. Lide

Submitted to the Department of Physics & Astronomy
on 2021-Apr-23, in partial fulfillment of the
requirements for the Bachelor of Science in Physics

Abstract

Using an 8th order symplectic integration routine, we develop a program which calculates the trajectories of N particles in a D-dimensional phase space. These trajectories are analyzed to determine the lifetime of the transient collision complex specifically for a K+K+Rb collision in 1 dimension. These results are compared with quasiclassical Rice-Ramsperger-Kassel-Marcus (RRKM) Theory lifetime approximations to further validate this theory. Additionally the Fast Lyapunov Indicator is calculated for the system to definitively determine under what conditions the reactants and products behave chaotically or regularly.

Thesis Supervisor: Prof. Nirav P. Mehta

Acknowledgments

Contents

Chapter 1

Introduction

Ultracold physical systems have been in the mainstream of cutting edge physics since 2001 when Eric Cornell and Carl Wieman at the University of Colorado at Boulder NIST-JILA lab and Wolfgang Ketterle at the Massachusetts Institue of Technology developed a gaseous Bose-Einstein condensate made of alkali atoms (Anderson et al. 1995). With this material, a large fraction of bosons occupy the lowest quantum state of the trapping potential, allowing experimentalists to directly observe quantum mechanical phenomena. Particularly, the wavefunctions of many of the atoms in the condensate can interfere, becoming apparent macroscopically.

In addition to allowing direct observation of quantum mechanical phenomena, ultracold physical systems such as Bose-Einstein condensates and single atom optical lattice traps allow sensitive control of chemical kinematics (Bell and Softley 2009). These experiments allow for a close study of the forms of the interaction potentials between the reactants. Furthermore, ultracold trapped ions can serve as the qubits of quantum computing systems. Quantum computers are able to solve certain computational problems significantly faster than their classical counterparts (Grumbling and Horowitz 2019).

In order to realize the full potential of these ultracold experiments, the few-body physics present in them must be understood. Inelastic collisions between ultracold magneto-optically trapped atoms can lead to the atoms gaining sufficient kinetic energy to escape the trap. Ritchie et al. state that at low trap laser intensities, trapped ^{7}Li atoms can collide to cause a trap loss rate of $10^{-10} \mathrm{cm}^3/\mathrm{s}$ (Ritchie et al. 1995). When trapped atoms are lost due to collisions, the efficiency of the trap is decreased. To better understand these collisions which lead to trap loss, we classically simulate reactions between two potassium atoms and one rubidium.

Quantum mechanical calculations certainly represent the true nature of reality better than classical ones and would provide the most accurate numerical results, provided computational power is sufficiently high. However, the 3-body collision complex of closely interacting K+K+Rb atoms supports a large number of states and a correspondingly large basis-set expansion (Soley et al. 2018) is required. Thus full quantum mechanical calculations demand high computational power and long computing time. Additionally, while the atoms are closely interacting, large magnitudes of potential energy are converted to kinetic, meaning that classical physics provides a strong approximation to the true lifetimes of these particles while they are in the 3-body collision complex.

In order to develop a deeper understanding of these 3-body reactions, we compare collision complex

lifetimes calculated classically with Rice-Ramsperger-Kassel-Marcus (RRKM) Theory approximations to the lifetime, as James F.E. Croft and John L. Bohn do in their paper entitled *Long-lived complexes and chaos in ultracold molecular collisions* (Croft and Bohn 2014). Perhaps no previous work has been as influential to this work as Croft and Bohn's. The RRKM approximation is a semi-classical method which employs knowledge of the energy level spacing of the system and is described in detail in Section 2.4 [1].

Furthermore, we apply a tool called the Fast Lyapunov Indicator (FLI) to definitively determine whether the system is exhibiting chaotic behavior at different times. This tool tells us that, even in 1-dimension, the 3-body system of K+K+Rb can behave highly chaotically at sufficiently low energies. The FLI also shows a clear and distinct shift in behavior when the system deteriorates into its products, corresponding to highly chaotic behavior in the collision complex, and very regular behavior at all times thereafter.

---

[1] For further, more in depth reading regarding RRKM theory applied to alkali metal collisions and their lifetimes, see (Christianen et al. 2019).

Chapter 2

Background Theory

2.1   Morse Potential

To model the two-body interactions between pairs of atoms, we use a simple but well understood potential: the Morse Potential. This interaction potential takes the form

$$V(r) = D_e(e^{-2(r-r_e)a} - 2e^{-(r-r_e)a}).\tag{2.1}$$

where D_e is the depth of the potential well, a is a parameter which governs the width of the well, r_e is the equilibrium separation of the atoms, and r is the separation of the two atoms in question (Morse 1929). The values used for these parameters are given in Table 2.1.

	K_2	Rb_2	KRb
$D_e(E_h \times 10^{-2})$	2.007 243	1.807 0	1.904 738
r_e (Å)	7.476	7.980	7.861

Table 2.1: The values of the equilibrium separations r_e are calculated while the well depths D_e are measured experimentally (Byrd et al. 2010).

For the a parameter, the vibrational constants of the dimers were matched to the Taylor expansion of the Morse Potential about the bottom of the well. The procedure goes as follows. First, Taylor expanding the Morse Potential gives

$$V(r) = D_e \left(e^{-2(r-r_e)a} - 2e^{-(r-r_e)a}\right) = -D_e + D_e a^2 (r - r_e)^2 + \ldots\tag{2.2}$$

At the infinitesimal limit $(r - r_e) \to 0$, the bottom of the Morse Potential well can be perfectly modeled as a quadratic. The coefficient of the quadratic term in the previous equation can then be taken as the force constant of this quadratic approximation of the bottom of the well as shown in Eqn 2.3.

$$D_e a^2 (r - r_e)^2 = \frac{1}{2}\mu\omega_e^2(r - r_e)^2\tag{2.3}$$
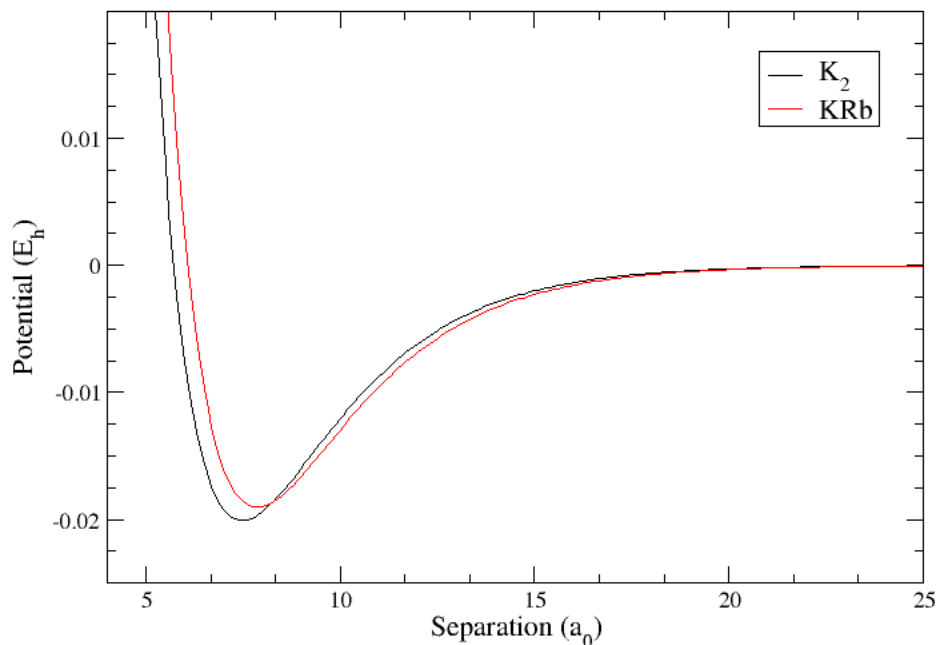
Morse Potential

Figure 2-1: Plotted (in atomic units) are the pairwise Morse potential interactions between two potassium atoms as well as the interaction between one potassium atom and one rubidium atom as described by Eq. 2.1. As the separation between the atoms goes to 0, the potential increases drastically.

The frequency for simple harmonic motion, $\sqrt{\dfrac{k}{m}}$ is applied as such

$$\omega_e = \sqrt{\frac{2D_e a^2}{\mu}} \tag{2.4}$$

where μ is the two-body reduced mass of the dimer. Solving for the a parameter yields

$$a = \omega_e \sqrt{\frac{\mu}{2D_e}}. \tag{2.5}$$

The results of this calculation for K_2 and KRb, as well as the constants required, are shown in Table 2.2.

	K_2	KRb
ω_e (cm^{-1})	92.021	75.5
a (a_0^{-1})	0.3949	0.390

Table 2.2: The atomic mass of Potassium is 39.0983 amu and the mass of Rubidium is 85.4678 amu (NIST 2018b) (NIST 2018c).

2.2 The Integration Routine

For this work, we employ an 8th order symplectic integration routine developed by Schlier and Seiter specifically for simulating triatomic molecules (Schlier and Seiter 2000). A symplectic integrator is defined as a numerical integration method that solves Hamiltonian systems while preserving phase space volume (Vogelaere 1956). The advantage of using a symplectic integrator is that the magnitude of the numerical error in the energy is the same after having integrated through some time t_1 and through time t_2 where $t_2 \gg t_1$. For problems involving chaotic systems (such as the transient 3-body collision complex present in this research) or situations in which we must integrate through very long times relative to time step size, the energy conserving property of symplectic integrators becomes increasingly vital. More well known integration routines such as Runge-Kutta are often not symplectic, which is why we do not use them for this work.

However, as shown in Section 3.1, even with a symplectic integration routine, some aspects of these collisions fail to converge no matter the time step used. For the most complex trajectories, the collision lifetime can vary as much as 50% for certain integrator time steps. Thus, using a symplectic integrator does not save us from all sensitivity to initial conditions. In other words, the use of a symplectic integrator does not guarantee a perfect calculator for chaotic motion.

2.3 Jacobi Coordinates

Given a set of three Cartesian coordinates, $x_1, x_2,$ and x_3 a set of corresponding Jacobi coordinates is defined by (Cornille 2003)

$$y_1 = \sqrt{\frac{\mu_{12}}{\mu}}(x_1 - x_2) \tag{2.6}$$

and

$$y_2 = \sqrt{\frac{\mu_{12,3}}{\mu}}\left(\frac{m_1 x_1 + m_2 x_2}{m_1 + m_2} - x_3\right). \tag{2.7}$$

The reduced masses here are given by

$$\mu_{12} = \frac{m_1 m_2}{m_1 + m_2}, \tag{2.8}$$

$$\mu_{12,3} = \frac{(m_1 + m_2)m_3}{M} \quad \text{and,} \tag{2.9}$$

$$\mu = \sqrt{\frac{m_1 m_2 m_3}{m_1 + m_2 + m_3}} \tag{2.10}$$

where m_i is of course the mass of the ith particle and M is the total mass as usual.

Using this set of definitions, and also assuming the frame of the center of mass, the hyper-radius R is defined as
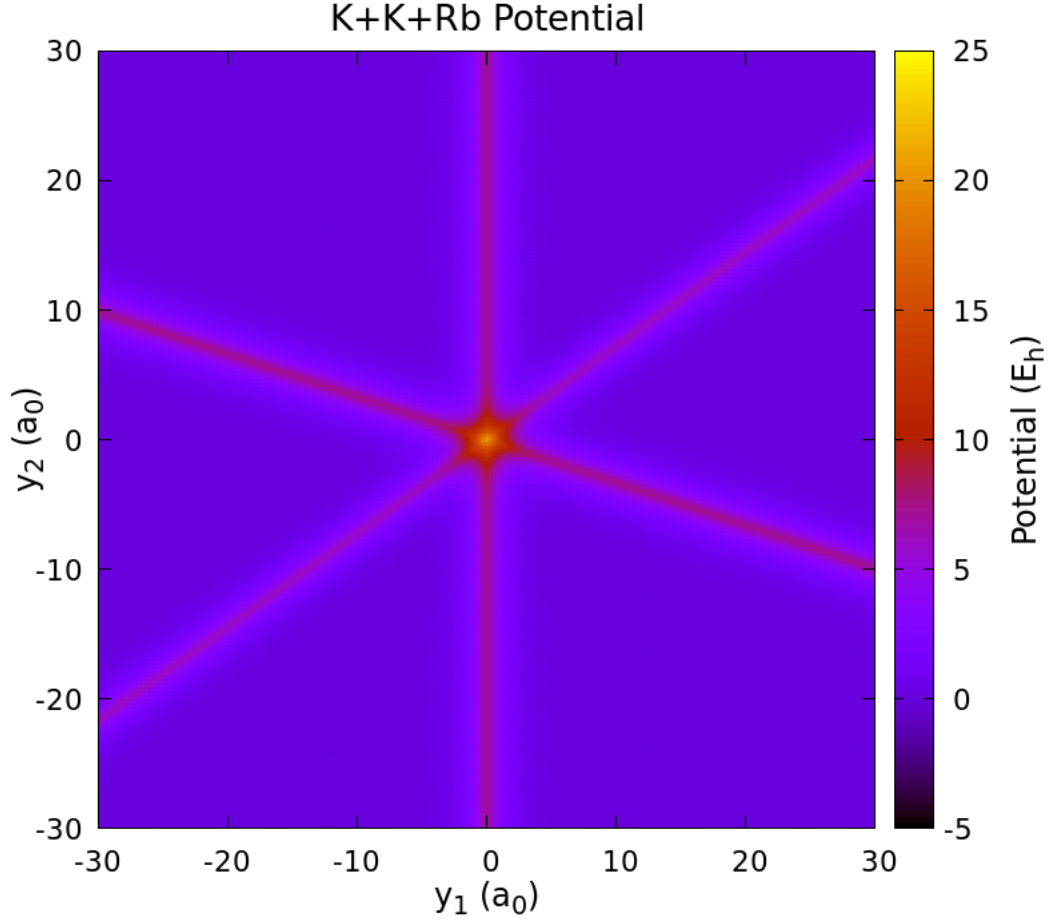
$$R = \sqrt{y_1^2 + y_2^2}. \tag{2.11}$$

Figure 2-2: Plotted above is the 3-Body Morse potential of a K + K + Rb system with the Jacobi coordinates on the x and y axes, as defined in Eqns. 2.5 and 2.6. For this plot, particle 1 is rubidium and particles 2 and 3 are potassium. The bright lines of high potential energy are the lines where two of the atoms' Cartesian coordinates are equal and the atoms coalesce. Specifically, the vertical line corresponds to $x_1 = x_2$ (a KRb dimer), and continuing clockwise the other lines correspond to $x_2 = x_3$ (a K_2 dimer) and $x_1 = x_3$ (another KRb dimer).

Analogously, the hyper-angle θ is defined as

$$\theta = \tan^{-1}\left(\frac{y_2}{y_1}\right). \tag{2.12}$$

Throughout this paper the regions near the bright lines of high potential (as shown in Figure 2-2) will be referred to as "arms" or "entrance channels". For example, the area near the vertical line shown in Figure 2-2 is called the KRb entrance channel. For $y_1 \approx r_e^{(KRb)}$ and $y_2 >> y_1$ the system is effectively a KRb dimer and a lone K atom at a sufficiently large distance such that it is only weakly interacting with the KRb dimer. Similarly, at large hyper-radius along the K_2 arm (the first line in the clockwise direction from vertical in Figure 2-2), the system is accurately described as a lone Rb atom which weakly interacts

with a bound K_2 dimer.

Furthermore the regions of the 3-body potential surface in which all three particles are closely interacting at small R will be called the collision "cauldron". See Figure 2-3. In the cauldron, potential energy is negative and very high kinetic energies can be achieved by the reactants. Thus the motion is well approximated by classical calculations in the cauldron. Additionally, the motion in the cauldron is highly chaotic due to the asymmetry of the potential.
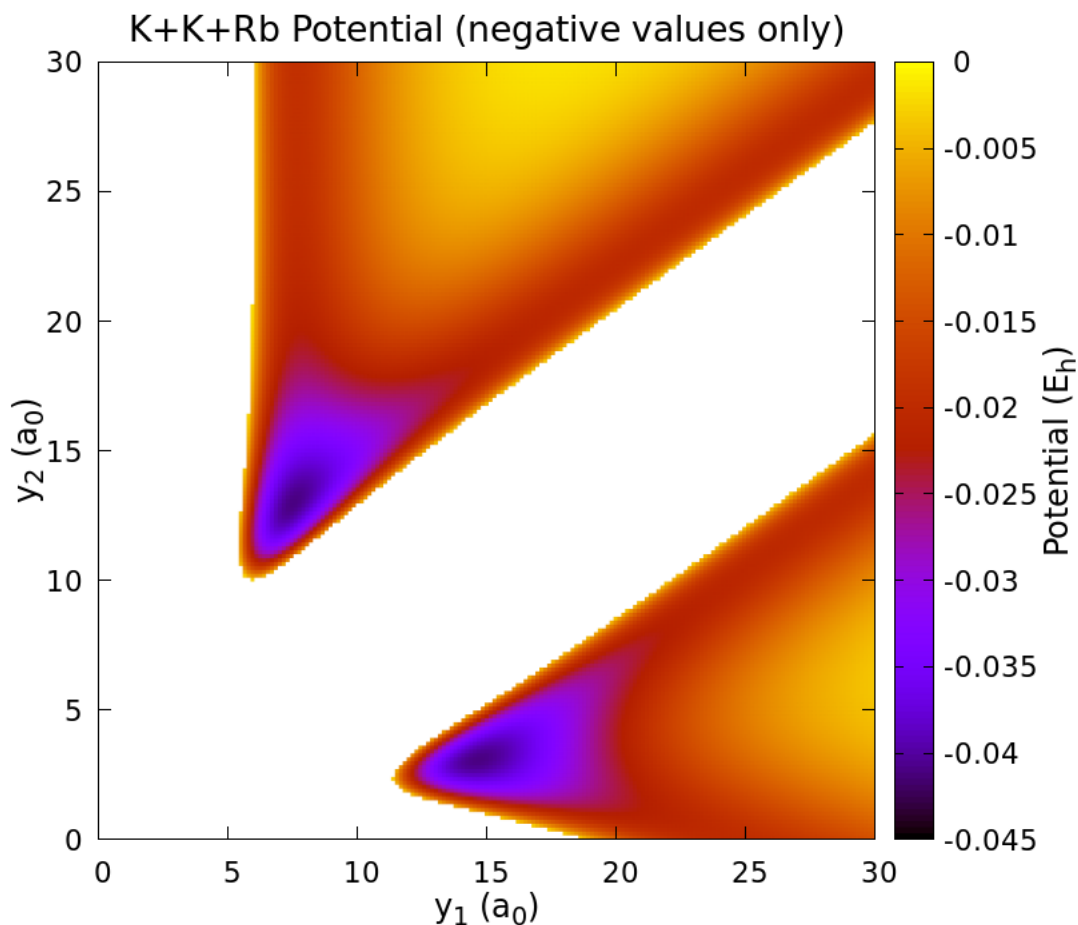

Figure 2-3: This is the same plot as Figure 2-2 (with different ranges of y_1 and y_2) but with only the negative values of the potential shown in color so that the shape of the cauldron can be seen. Inside the regions of lowest potential energy (blue and black areas), all three particles in the system are very closely interacting. By definition, it is in these cauldrons that the transient 3-body collision complex lives its entire life. And for our calculation, it's only the upper potential well that is ever explored since the pair-wise potential does not allow the permutation order of the particles along the real, Cartesian line to change at the energies we consider.

2.4 Rice-Ramsperger-Kassel-Marcus Theory

The Rice-Ramsperger-Kassel-Marcus transition state theory of the rate constant k of atomic reactions is given by (Levine 2005)

$$\tau = k^{-1} = \frac{2\pi\rho_{3B}(E)}{N_0(E)} \tag{2.13}$$

where ρ_{3B} is the 3-body density of states (DOS), N_0 is the number of open exit channels for the collision (ie. quantum states energetically available to the collision fragments) and τ is the semi-classical approximation of the lifetime of the transient 3-body collision complex. A distinction and emphasis must now be made between the classical exit channels which have been previously discussed, and the quantum exit channels quantified by N_0. These are not the same, of course. The number of classical exit channels can easily be counted by inspecting Figure 2-2. There can only be 6 permutations of 3 atoms and this number of classical exit channels is not dependent upon anything other than the number of atoms in the system. Moreover, only two of these classical exit channels are available at ranges of energies which we study, since the particles cannot move through each other and change permutations at these relatively low energies. However, the quantum exit channels N_0 depend closely on the energy of the system. The number of quantum exit channels can be calculated as an integral over the 2-body density of states ρ_{2B}

$$N_0(E) = \int_{-D_e}^{E} \rho_{2B}(E')dE'. \tag{2.14}$$

Thus, N_0 can drop all the way to unity at the lowest temperatures, increasing the quantum lifetime approximation. In contrast, at room temperature the number of quantum exit channels can be quite large, making lifetimes very short.

With each close interaction in the collision complex, the energy of the system is effectively randomly distributed among the degrees of freedom in phase space. The higher the 3-body density of states, the closer together the eigenstates in the collision complex are, meaning there is a higher chance that a random reassignment of energy will result in a state that is in the collision complex. Conversely an increase in possible ways that the complex can decay (which is determined by an increase in N_0) will correspond to a higher chance that a random reassignment of energy will result in a state which exits the collision cauldron. Thus, the semi-classical approximation for the lifetime is directly proportional to the DOS ρ and inversely proportional to N_0.

2.5 Chaos Indicator

The motion of the 3-body collision complex inside the cauldron is highly chaotic, often exploring nearly the entirety of phase space available to the system. To quantify this behavior, and to definitively determine whether or not chaos is actually present, Lyapunov exponents are calculated. Put simply, the Lyapunov exponent is the rate at which two systems with very slightly different initial values diverge from one another. Since slightly different initial conditions lead to trajectories in chaotic systems diverging exponentially in time, a positive, non-zero Lyapunov exponent is an indication that chaos is present in the system.

Consider a system with phase space coordinates (Meyer 1986)

$$\vec{\gamma} = \begin{pmatrix} \vec{x} \\ \vec{p} \end{pmatrix} \tag{2.15}$$

where $\vec{x}$ and $\vec{p}$ are vectors (with size equal to the number of degrees of freedom) containing all of the position and momentum coordinates needed to fully describe the system in phase space. If it is then assumed that this is a Hamiltonian system, the equations of motion describing $\vec{\gamma}$ are

$$\frac{d\vec{x}}{dt} = \frac{\partial H}{\partial \vec{p}} \quad \text{and} \quad \frac{\partial \vec{p}}{\partial t} = -\frac{\partial H}{\partial \vec{x}}. \tag{2.16}$$

Or, written more compactly,

$$\dot{\vec{\gamma}} = \boldsymbol{J} \overrightarrow{\left(\frac{\partial H}{\partial \vec{\gamma}} \right)}, \tag{2.17}$$

where $\boldsymbol{J}$ is the anti-symmetric matrix defined as $\boldsymbol{J} = \begin{pmatrix} \mathbf{0} & \mathbf{1} \\ \mathbf{-1} & \mathbf{0} \end{pmatrix}$ [1] . Furthermore, the H derivate in Eqn 2.17 is a vector given by elements

$$\left(\frac{\partial H}{\partial \vec{\gamma}} \right)_i = \left(\frac{\partial H}{\partial \gamma_i} \right). \tag{2.18}$$

So far, we have only written Hamilton's equations in a slightly different way. To analyze the chaoticity of the system, we must define a deviation vector $\vec{v}$ as the difference between phase-space coordinates of trajectories which begin with very slightly different positions in phase space. Written explicitly, considering an initial trajectory characterized $\vec{\gamma_0}(t)$ and some other trajectory with altered initial conditions characterized by $\vec{\gamma}(t)$, the deviation vector is

$$\vec{v}(t) = \vec{\gamma}(t) - \vec{\gamma_0}(t) \tag{2.19}$$

The time evolution of the deviation vector is given by [2] Libert et al. (2011)

$$\dot{\vec{v}} = \boldsymbol{J} \frac{\partial^2 H}{\partial \vec{\gamma}^2} \vec{v}. \tag{2.20}$$

The second derivative of the Hamiltonian in the preceding equation is a matrix, just as the first derivative of the Hamiltonian with respect to the phase-space vector $\vec{\gamma}$ is a vector. The elements of this H derivative matrix are

$$\left(\frac{\partial^2 H}{\partial \vec{\gamma}^2} \right)_{i,j} = \frac{\partial^2 H}{\partial \gamma_i \partial \gamma_j} \tag{2.21}$$

where exactly half of the elements of $\vec{\gamma}$ are positions and the other half are momenta. Now we have all the tools we need to define our indicator of chaos, the Fast Lyapunov Indicator (FLI). While multiple forms

---

[1]Each of the elements of the anti-symmetric matrix is also an n-by-n square matrix where n is the number of degrees of freedom in phase space.

[2]For an example problem which illuminates the meaning of this equation, see Section 5.2 *Deviation Vector Example* in the Appendix.

of FLIs exist (Froescilé et al. 1997) we define our FLI as

$$FLI(t) = \frac{1}{t} \ln \frac{\|\vec{v}\|}{\|\vec{v_0}(t)\|}, \qquad (2.22)$$

where $\|\vec{v_o}\|$ represents the norm of the vector $\vec{v_0}$. In the long time limit, the FLI will tend towards 0 if the system is not chaotic, and will tend towards some positive value if the system does exhibit chaos (Meyer 1986).

Chapter 3

Calculations and Analysis

3.1   Integration Time Step

For any integration routine, using a time step that is small enough to capture the details of the trajectory is of utmost importance. This becomes especially true for chaotic behavior, as K+K+Rb reactions display in the 3-body cauldron for certain energy ranges. To insure that a small enough step size was used, a random set of initial conditions was chosen such that the system exhibited chaotic behavior inside the cauldron. This trajectory is shown in Figure 3-1a.

The lifetime of this trajectory was then calculated for a set of integrator time steps to ensure convergence. These results are plotted in Figure 3-1b.

While most trajectories converge for time steps $< 2 \times 10^{-5}$ ns, some of the longest and most chaotic trajectories fail to converge in time step at all. The same study as is done in Figure 3-1b is conducted again for another trajectory (shown in Figure 3-1c). Figure 3-1d displays the failure of this trajectory to converge at small time step. This is an artifact of the high degree of chaoticity demonstrated by the trajectory in question. For trajectories such as these, we must at times content ourselves with qualitative results.

3.2   Cutoff Hyperradius

In order to calculate the lifetime of the 3-body collision complex, an admittedly arbitrary choice must be made as to when the complex has officially broken up. The most obvious parameter to base this decision is the hyperradius (as defined in Eq. 2.11). In fact, this is the primary reason for calculating the hyperradius. But what hyperradius should be chosen as the signal of a dissolved collision complex? A small cutoff hyperradius R_{cutoff} excludes the slow oscillitory behavior of the system in the exit channel, but risks ending collisions that may have turned around in the exit channel. This would falsely lower the calculated collision complex lifetime. On the other hand, a large R_{cutoff} lowers the possibility of incorrectly ending the trajectory before it might've reentered the cauldron. However, a large cutoff hyperradius also counts the slow oscillations in the exit arm as part of the collision lifetime, effectively "watering down" the interesting physics that occurs in the cauldron.

In order to get a rough estimate of a sensible hyperradius to chose, the hyperradius of many trajectories

was plotted in time. Figure 3-2 shows the results of a subset of these trajectories. By inspecting this plot and four others like it, we were able to find that only 2 out of these 500 trajectories reached a hyperradius greater than 100 a_0 and returned to the collision complex cauldron. Thus, by setting the cutoff hyperradius to 150 a_0 we are able to safely say that very very few trajectories are prematurely terminated when they would have re-entered the cauldron. However, this value of R_{cutoff} counts a large amount of uninteresting exit arm oscillations, which dominates the calculated value of the lifetimes. Thus, we must develop a method to correct for this excess time, the procedure for which is described in Section 3.5.

3.3 Density of States

To calculate the two-body DOS, ρ, as a function of energy, we integrate a delta function selecting the correct energy level over all phase space and divide by the minimum area of regions of phase space, namely Planck's constant h. Thus the density of states for two bodies in one dimension is given by

$$\rho_{2B} = \frac{1}{h} \int_{-\infty}^{\infty} \delta(E - \mathcal{H}) dx dp. \tag{3.1}$$

where $\mathcal{H}$ is the Hamiltonian of the system and E is the total energy; x and p are position and momentum as usual. To simplify this expression, we multiply the argument of the delta-function by -1 which is allowed because delta-functions are even functions. Plugging the Hamiltonian into this new expression yields

$$\rho_{2B} = \frac{1}{h} \int_{-\infty}^{\infty} \delta \left(\frac{p^2}{2\mu} - (E - V(x)) \right) dx dp. \tag{3.2}$$

Now we define a change of variables $q = \frac{p}{\sqrt{2\mu_{2B}}}$ such that the DOS becomes

$$\rho_{2B} = \frac{\sqrt{2\mu_{2B}}}{h} \int_{-\infty}^{\infty} \delta \left(q^2 - (E - V(x)) \right) dx dq. \tag{3.3}$$

For any continuously differentiable function $g(x)$ it is possible to define the composition $\delta(g(x))$ as

$$\delta(g(x)) = \sum_i \frac{\delta(x - x_i)}{|g'(x_i)|} \tag{3.4}$$

where x_i is the ith root of the function $g(x)$. Therefore, the DOS can be written as

$$\rho_{2B} = \frac{\sqrt{2\mu_{2B}}}{h} \int_{-\infty}^{\infty} \left[\frac{\delta \left(q - \sqrt{E - V(x)} \right)}{2\sqrt{E - V(x)}} + \frac{\delta \left(q + \sqrt{E - V(x)} \right)}{2\sqrt{E - V(x)}} \right] dx dq. \tag{3.5}$$

Considering the definition of the delta function (Gel'fand and Vilenkin 2014)

$$\int_{-\infty}^{\infty} \delta(x) dx = 1, \tag{3.6}$$

16

we can factor out the common denominator and complete the integral over q to obtain

$$\rho_{2B} = \frac{\sqrt{2\mu_{2B}}}{h} \int_{E > V(x)} \frac{dx}{\sqrt{E - V(x)}}. \tag{3.7}$$

The results of this integral for K_2 and KRb are shown in Figure 3-3a.

The 3-Body DOS in one dimension is calculated similarly, as

$$\rho_{3B} = \frac{\mu}{h} \int_{\theta_0}^{\pi/2} d\theta \int_{D_e^{(3B)}}^{0} dE \Theta(E - V(r,\theta)). \tag{3.8}$$

Here $\theta_0 = \tan^{-1}(\mu/m_2)$ is the angle at which particles 2 and 3 coalesce and Θ is the Heaviside step function. The region of phase space which is integrated over is determined by the region which is accessible to the system. The system is confined to the slice of Jacobi space in which the particles are ordered (from left to right) particle 3, 2, and then 1. This corresponds to the upper right region in Figure 2-2. This ordering never changes throughout the collision when the system has sufficiently low initial energy. This is because the particles do not have enough energy to climb the high potential energy peaks which correspond to particle coalescence. Thus, there is no need to divide ρ_{3B} by some integer which would correct for identical particles changing positions. The result of the Eq. 3.8 is shown in Figure 3-3b.

3.4   Number of Open Exit Channels

The total number of quantum exit channels N_0 that the 3-body complex has available is simply a sum of the number of open quantum exit channels for individual K_2 and KRb arms

$$N_0(E) = N_0^{(K_2)}(E) + N_0^{(KRb)}(E). \tag{3.9}$$

Because of the definition of the DOS, ρ is simply the energy derivative of N_0 (Christianen et al. 2019). So the previous equation becomes

$$N_0(E) = \int_{-D_e^{(K_2)}}^{E} \rho_{K_2} dE' + \int_{-D_e^{(KRb)}}^{E} \rho_{KRb} dE'. \tag{3.10}$$

The calculation is shown in Figure 3-4.

3.5   RRKM vs Classical Lifetimes

With the 3-body density of states and the total number of open quantum exit channels N_0, we can use Eqn. 2.13 to determine an approximation to the lifetime of K+KRb collisions as a function of energy. Using the curves plotted in Figure 3-3b and Figure 3-4, we obtain the black curve in Figure 3-5. Inspecting this curve tells us that RRKM theory suggests that the collision complex lifetimes will be roughly constant (at roughly 0.1 ns) until the collision energy reaches approximately 100 K. The collision energy is defined as the kinetic energy in the y_2 direction or the kinetic energy defining the rate at which the KRb dimer and the lone K atom approach each other, before entering the collision complex cauldron.

However, the behavior exhibited by the RRKM lifetime approximation curve is vastly different from a lifetime curve obtained through classically calculated trajectories. These classically calculated trajectories are initiated at a hyperradius of 100 a_0 at precisely the bottom of the KRb entrance channel, such that the KRb dimer is at perfect equilibrium and the atoms are not oscillating with respect to one another at all. As opposed to the RRKM approximation, these classically calculated trajectories suggest that the collision complex lifetime increases without limit at the collision energy goes to 0.

This behavior has a simple explanation, with a surprisingly difficult solution. Of course, the classically calculated trajectory lifetimes include time spent in the cauldron (which is the part of the trajectory we care about). But these lifetime calculations also include time spent travelling down the entrance arm and back out the exit arm. So at the lowest collision energies, the classically calculated lifetimes are dominated by this time spent in the arms. Put in different words, when the initial KRb dimer approaches the lone K atom slowly, most of the classically calculated collision lifetime consists of this slow motion (on approach and in fact on exit as well), not the actual time spent inside the 3-body collision cauldron. This is why the classically calculated lifetimes continue to increase at the lowest collision energies.

In order to consider only the time spent in the cauldron, one might naively attempt to bring the initial hyperradius of the calculation and the final, cut-off hyperradius closer to the cauldron. This would exclude the slow oscillatory behavior in the entrance and exit arms. But what radius is the correct one to choose? All choices of initial and final hyperradius are arbitrary. Furthermore as discussed in Section 3.2 *Cutoff Hyperradius*, bringing the cutoff hyperradius too close risks prematurely terminating some trajectories which might re-enter the cauldron. This problem could be overcome by letting the collision continue until some very large hyperradius R_∞ is reached, saving the values of the hyperradius at all time steps so that all the time after the last close encounter of the reactants could be thrown out. However, this is a memory intensive solution.

Another approach to finding the fraction of the classically calculated lifetimes actually spent inside the collision complex is to calculate the time spent in the entrance and exit arms and subtract. To do this, we can imagine that the system travels down the entrance channel and immediately begins to travel back out again. Using the potential energy surface in Figure 2-2, it is possible to find the potential energy at every point on the Jacobi surface plot. Thus we can find the kinetic energy throughout this entire "one-bounce" trajectory since, of course, total energy is still conserved. Armed with complete knowledge of the kinetic energy during this imaginary trajectory, it is now possible to calculate the speed of the 3-body system through Jacobi space. Put simply, it is possible to calculate the amount of time a very simple, idealized system spends approaching and leaving the collision complex cauldron. This is the procedure which led to the blue curve labeled "Arm Time Approx." in Figure 3-5. The exact integral used to produce 3-5 is

$$t_{arms} = \int_{R_i}^{R_{\text{turn}}} \frac{dx}{v(x)} + \int_{R_{\text{turn}}}^{R_f} \frac{dx}{v(x)}, \tag{3.11}$$

where the exact expression for the speed, $v(x)$ is substituted as such

$$t_{arms} = \int_{R_i}^{R_{\text{turn}}} \sqrt{\frac{mu}{2(KE_i + V_i - V(x))}} dx + \int_{R_{\text{turn}}}^{R_f} \sqrt{\frac{mu}{2(KE_i + V_i - V(x))}} dx. \tag{3.12}$$

18

To be explicit, the initial hyperradius, R_i and final hyperradius, R_f were chosen to be $100a_0$ and $150a_0$ respectively, in order to match the values in the full classically calculated trajectories. Furthermore, the system was imagined to travel directly down the KRb entrance arm to a hyperradius of $5a_0$, this is the value of R_{turn}. At this point of closest approach, the system immediately and spontaneously turns around and travels directly back out the KRb arm. An exact numerical calculation would need to find the exact inner hyperradius turning point, as defined by the total energy of the system, and integrate up to this point. Furthermore, since all of the full classically calculated trajectories end up exiting the K_2 arm, this is the direction that the imaginary "one-bounce" should take as well. However, the previously presented calculations are far simpler. Future work should seek to make the above mentioned adjustments.

Finally it is a simple matter of subtracting this approximation of the time spent in the arms off of the full classical trajectory calculations. The difference is shown in the red curve, labeled "Cauldron Time " in Figure 3-5. The fact that the blue arm time approximation curve in Figure 3-5 is larger than the actual calculated trajectory lifetime is indicative of the faults in the previously mentioned arm time calculation. Thus the cauldron time (the difference between the classically calculated lifetimes and the arm time approximations) is negative for ultracold energies. Of course, this is not physically accurate.

Obviously there is significant discrepancy between the RRKM approximation lifetimes and the classically calculated cauldron times. At certain energies, there are in fact two orders of magnitude of difference. We are yet unable to pinpoint a single stand alone cause for this discrepancy, but some candidates exist. Perhaps the arm time approximation described above does not accurately represent the time that the system spends in the arms. In fact, it is almost impossible for the system to exit the cauldron with no oscillation in the exit arm. In other words, the product K_2 dimer will almost always have some internal oscillation kinetic energy. Taking this into consideration would increase the blue arm time curve in Figure 3-5 for all energies. This would also lower the red difference curve, bringing the classically calculated cauldron time closer to the RRKM prediction.

Furthermore, as was shown in Figure 3-1d, snarled chaotic trajectories do not converge well with respect to integrator time step size. However, on this log-log plot, the correction would not appear as a major difference. Even trajectories which are not converged in time step size differ from the same calculation with a different step size by 40%, a very large sounding number, but certainly not enough to correct a 1000% discrepancy (as is the case for some collision energies in Figure 3-5.

A final feature of the rich Figure 3-5 worth understanding is the reason that the black RRKM approximation curve begins to drop off noticeably at a collision energy of roughly $100K$ and not before. This drop occurs only at this high of kinetic energy because the potential energy of the system dominates the total energy. That is, for collision energies $< 100K$, only the first 10 energy levels in the K_2 arm are accessible. This means that the value of $N_0^{(K_2)}$ is constant until the energy becomes high enough to explore more than the first 10 energy levels of the K_2 exit arm. The first ten quantum energy levels of the K_2 dimer are shown in Figure 3-6.

To demonstrate how the energy of the system is distributed into the vibrational degree of freedom in the exit channel (and thus the value of N_0), the internal energy of the K_2 dimer is recorded for many trajectories of varying initial conditions. 1000 trajectories are calculated with 10 K of kinetic energy entirely in the y_2 direction, as before. But now, the initial position is altered randomly for each trajectory

Level	Energy ($\times 10^{-2} E_h$)
1	-2.0002
2	-1.9860
3	-1.9719
4	-1.9578
5	-1.9439
6	-1.9299
7	-1.9160
8	-1.9022
9	-1.8884
10	-1.8746

Table 3.1: Quantum energy levels for the K_2 dimer. These values were calculated using code written by Dr. Nirav Mehta. Code can be found at https://github.com/mehta-group-at-trinity-university/1D-Schrodinger-bsplines-BOUND-STATES.

such that they all begin with an initial hyperradius R_i of 100 a_0, but they do not begin at the very bottom of the KRb entrance channel. Instead, some amount of internal potential energy is granted to the initial KRb reactant. These trajectories are then allowed to collide in the collision complex cauldron and escape out of the K_2 arm. Finally the trajectories are binned to display what quantum energy levels are available to them. That is, how many quantum energy levels are of lower energy than the internal energy of the K_2 product dimer. The results of this procedure are shown in Figure 3-7.

To explore how the energy of the system is distributed into the vibrational degree of freedom in the exit channel, Figure 3-7 is remade with higher collision energy. This plot is shown in Figure 3-8. The number of energetically available quantum levels begins to increase at roughly 50 K because this is the energy spacing near the bottom of the K_2 well. For all collision energies below 50 K, exactly the first 10 of the quantum energy levels are accessible to the K_2 product dimer. The reader will recall that the reason that the RRKM theory lifetime approximation begins to dip at a collision energy of 100 K is because at this energy, the semi-classically calculated value of open quantum exit channels N_0 begins to increase. Analogously, the classically calculated trajectories of Figure 3-7 and Figure 3-8 begin to have enough internal energy such that more quantum energy levels become accessible.

3.6 Fast Lyapunov Indicator

As Equation 2.22 states, the deviation vector $\vec{v}(t)$ determines the value of the FLI. However, we must choose what initial values to give this vector. Values that are too big might risk that the auxiliary trajectory which the deviation vector points to exits the cauldron along an entirely different arm than the original trajectory, even if little chaos is present. This would make the value of the FLI non-zero in the long time limit despite there not being actual chaos present, a false positive. On the other hand, too small of an initial deviation vector increases the duration of the collision which must be calculated before the FLI converges to some positive value. This is costly for these already computationally expensive calculations. Furthermore, in collisions which have enough energy to escape the cauldron, there is only a finite time of chaotic behavior before the trajectories escape and exhibit integrable behavior, leading to FLIs equal to 0. Luckily, as Figure

3-9 shows, within a reasonable range of initial values for the deviaiton vector, the FLI is not sensitive to the particular initial value, and converges well as time goes to infinity.

In addition to a fair degree of insensitivity to initial values in the deviation vector, the FLI does not seem to be nearly as sensitive to step size as the exact trajectories are. That is, at sufficiently large step size, the exact trajectory that is calculated can take an entirely different path through phase space and can exit the cauldron at times which vary by factors of 100%. However, when the step size is large and the calculated trajectory differs from the true trajectory, the deviation vector seems to point to an auxiliary trajectory which (even in the long time limit) differs from the true auxiliary trajectory by the same amount. Figure 3-10 demonstrates this behavior by plotting the FLI as a function of time for various integrator step sizes, xdt.

The purpose of the FLI is to indicate the presence of chaos. Since two chaotic trajectories with similar initial conditions (separated by the values of the deviation vector) will grow more and more distant as time passes, the FLI will converge to some positive, non-zero value in the long time limit. However, the separation between two regular trajectories, and thus the magnitude of the deviation vector, will remain constant in the long time limit, meaning the FLI will trend towards zero as $1/t$ (see Eqn 2.22). Thus, if the FLI is plotted for a trajectory which exhibits both chaotic and regular behaviours for different times, we should see a noticeable shift in the behavior of the FLI at the moment the behavior changes from chaotic to regular. One such trajectory is one that begins inside the cauldron, but with just enough kinetic energy to escape after some amount of time. For the time spent inside the collision complex cauldron, the FLI should hover around a non-zero positive value, as it does in Figures 3-9 and 3-8. Then, at the moment the trajectory leaves the cauldron and begins to exhibit regular, integrable, oscillatory behavior as it travels down the exit arm, the FLI should begin smoothly tending towards 0. This is exactly what is observed numerically, as shown in Figure 3-11.

In future work, this noticeable shift in the behavior of the FLI could be used to distinguish between cauldron and arm time. That is, instead of making an approximation of the armtime, as described by Eqn. 3.12, we could define the point which separates the behavior of the FLI as the last moment of the cauldron time. The only trick would be developing an algorithm which recognizes this change in the qualitative behavior of the FLI. One method would be to, at all time steps, try to fit a form of the tail of the FLI curve after the system exits the cauldron. We believe the form of this continually diminishing tail is proportional to $1/t$, however this needs validating. This $1/t$ dependence would certainly be true if $\|\vec{v}\|$ were constant in time, but we are not confident of this. Once the residual in the fit of the FLI curve to a function of this form is sufficiently low, the algorithm decides that the system is exhibiting regular behavior, and has thus exited the cauldron at some prior time. With the curve fitted to the calculation of the FLI, determining the moment of exit is a simple matter of finding the latest time at which the difference in the fitted curve and the calculated FLI values is sufficiently high (representing the last moment that the FLI was not trending towards 0).

However, the behavior show in Figure 3-11 is special. For purely regular trajectories, the FLI curve has no noisy behavior which hovers around a finite value, as is the case for the initial period of time in Figure 3-11. Plotted in Figure 3-12 is the FLI calculated for a simple harmonic oscillator. The FLI trends directly towards 0 with only a few bumps corresponding to the moments where each of the two trajectories

represented by the deviation vector are on opposite sides of an extremum of the oscillation.

Based on the same reasoning which describes the behavior of the FLI in Figure 3-11, we would expect that for collisions which begin in the collision complex, those trajectories which escape will have FLIs that tend towards 0 in the long time limit. Conversely trajectories which are not given enough kinetic energy to escape the cauldron, and are thus restricted to chaotic motion for all time, will have FLIs that converge to some non-zero value. Figure 3-13 depicts this feature of the FLI.

The trajectories which have total energies less than the K_2 well depth (equal to -2.01×10^{-2} E_h) are confined to the cauldron, because they have no energetically available arms out of which to escape. However, once the K_2 exit channel becomes available to the system (i.e. the total energy becomes $E > D_e^{(K_2)}$) the fraction of the total collision time spent in the cauldron (the red curve) begins to drop. These trajectories escape the cauldron at some time before the calculation is terminated. To emphasize, all of the trajectories shown in Figure 3-13 are calculated for 1.5 ns of collision time, and are allowed to continue well beyond the cutoff hyperradius mentioned earlier. So, the red curve in Figure 3-13 dropping to values well below 1 implies trajectories that escaped the cauldron and slowly oscillated out to large hyperradius for the remainder of the allotted 1.5 ns collision time. This increase in predictable exit arm oscillation behavior is reflected in the mirrored drop in the final value of the FLI for these collisions which escaped the cauldron.

Hopefully, future work will be able to reproduce Figure 3-13 at higher resolution (more values for total energy). Furthermore, the trajectories which would make up the individual points in this plot would be run for longer so that the recorded FLI value at the end of the simulation has had more time to converge. We expect this longer run time would lead to an effect of "smoothing out" the black FLI curve in Figure 3-13 for energies less than the K_2 well depth by allowing the FLI to converge to some common value for these trajectories. It would then be interesting to see if the value were exactly equal for all of these trajectories (with total energy less than the K_2 well depth), or if there are specific energy values that explore special regions of phase space where trajectories are not chaotic (if these exist).

Additionally, future work might plot the value of the FLI at the moment that the system escapes the 3-body collision complex to compare with the long-time limit of the FLI for those trajectories which are energetically bound to the cauldron forever. Currently, some of the information in Figure 3-13 is clouded by the fact that for trajectories which escape the cauldron early on in the simulation (and thus have small values for the fraction of the time spent in the cauldron), the FLI has more time to decay smoothly to 0 as shown in Figure 3-11. By plotting the FLI at the moment of the escape, more may be learned about the nature of the trajectories which lead to large peaks in the black FLI curve of Figure 3-13. Furthermore, plotting this earlier value of the FLI might show resonances in energy, or signal some fractal nature present in this plot.

Regardless of the physics yet to be uncovered by a more detailed version of Figure 3-13, the current version lets us make some conclusions. Studying this figure and Figure 3-11 tells us that the FLI is a forgiving and useful tool which can definitively say whether a system is acting chaotically or not. This tool can be used to distinguish between chaotic behavior in the cauldron and integrable behavior in the exit arms, allowing for more accurate collision complex lifetime calculations.
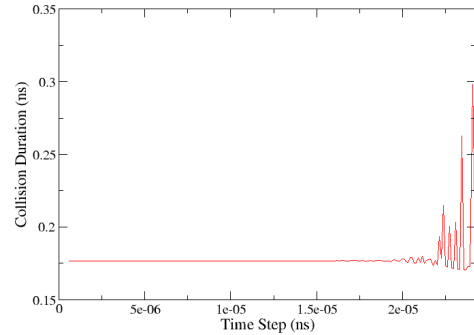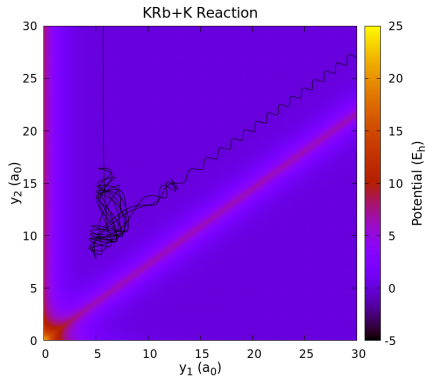
(a) KRb+K reaction with $KE_i = 1\ K$ in the $-y_2$ direction.

(b) The lifetime of the trajectory in Figure 3-1a calculated for a range of integrator time steps.
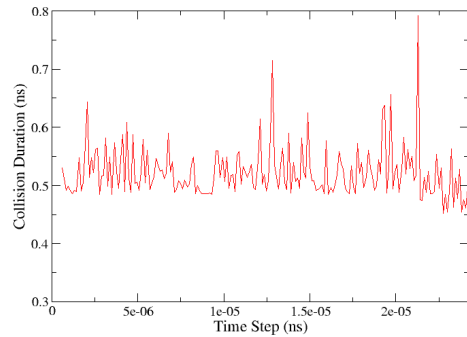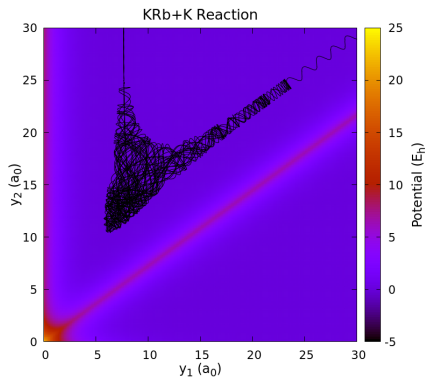
(c) KRb+K reaction with $KE_i = 0.1\ K$ in the $-y_2$ direction.

(d) The lifetime of the trajectory in Figure 3-1c calculated for a range of integrator time steps.

Figure 3-1: For both of the trajectories in Figure 3-1a and Figure 3-1c, a time step of $4.838 \times 10^{-6}\ ns$ was used and the systems were initiated at $R_i = 100\ a_0$ and $\theta_i = 1.49412$. The only difference between the two plots is the amount of initial kinetic energy given to the system. In Figure 3-1a, $KE_i = 1\ K$ while in Figure 3-1c, $KE_i = 0.1\ K$. In both cases, all of the kinetic energy is directed in the $-y_2$ direction. Both of these reactions are described by KRb+K → K_2+Rb. At a time step of roughly $< 2 \times 10^{-5}\ ns$, the lifetimes begin to become inaccurate in Figure 3-1b. To ensure fidelity, a time step of $10^{-5}\ ns$ is chosen to run the remainder of the integrations in this work. Since the collision in Figure 3-1a is chaotic inside the collision complex "cauldron", it is assumed that this time step will be sufficiently small for any trajectory of this system.
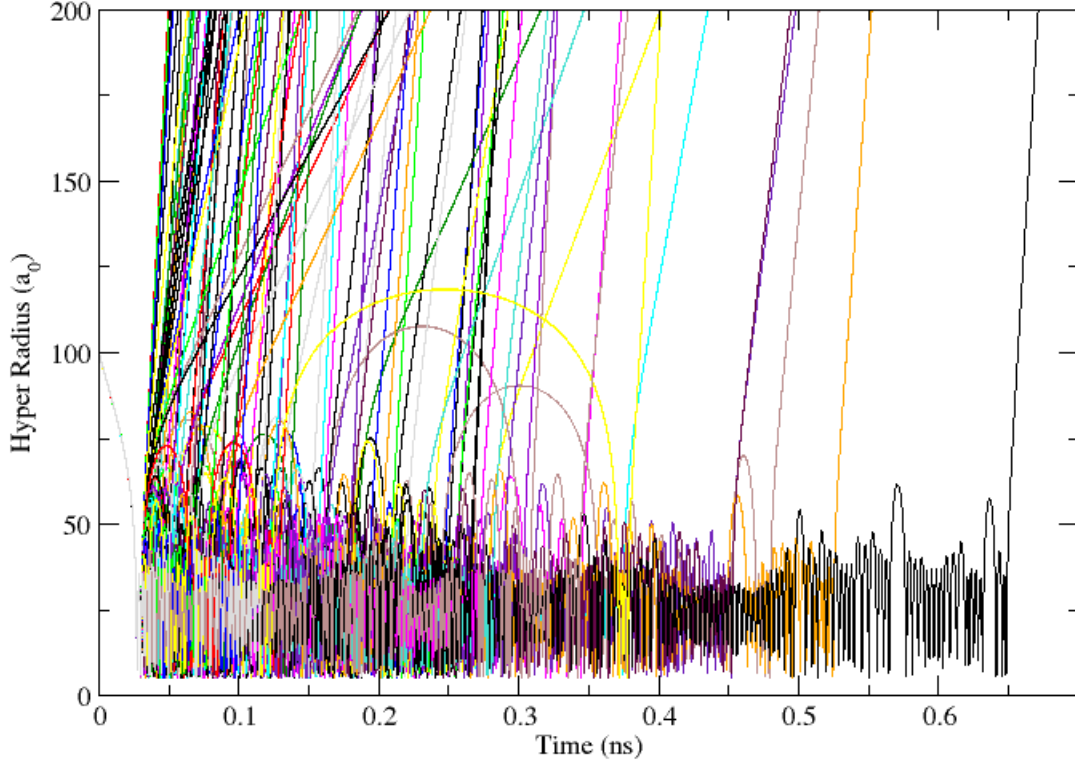
Figure 3-2: Plotted above are 100 trajectories of various initial positions near the bottom of the two-body KRb entrance arm. Each trajectory was given $1K$ of kinetic energy in the y_2 direction. In addition to the primary purpose of this plot to demonstrate a reasonable value for R_{cutoff}, another interesting feature is the slopes of these lines after the system exits the collision complex. These slopes of these "exit lines" can be divided into two bins, one with slopes near 200 $a_0/0.05$ ns and one much less populated bin with slopes near 100 $a_0/0.2$ ns. This far less common slope corresponds to the system exiting in the KRb arm. Since the well depth of the KRb channel is higher, systems which exit this arm have less kinetic energy on their way to infinite hyperradius. Naturally, the steeper exit lines correspond to the system exiting the K_2 arm. Of course, not all of the slopes in either bin are exactly equal because in both exit arms, the systems can have a continuum of 2-body vibrational energies. The higher the frequency of these oscillations, the less of the system's energy is kinetic energy directly in the hyper-radial direction and the smaller the slope of the exit line shown on this plot.

24
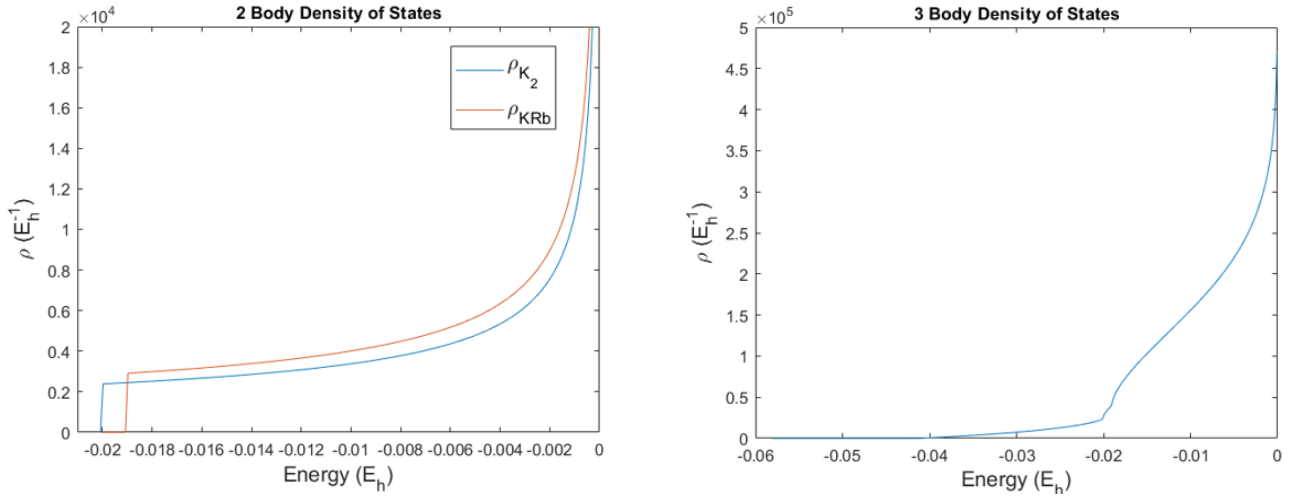
(a) The 2-body DOS calculated according to Eqn. 3.7.

(b) The 3-body DOS calculated according to Eqn. 3.8.

Figure 3-3: The first non-zero value of the each 2-body DOS in Figure 3-3a occurs at exactly the corresponding well depth, as expected. The 3-body DOS is non zero for energies lower than either of the two body well depths because the 3-body well depth is lower than either of the individual depths. However, there are two spikes in the 3-body DOS where these two body wells become accessible.
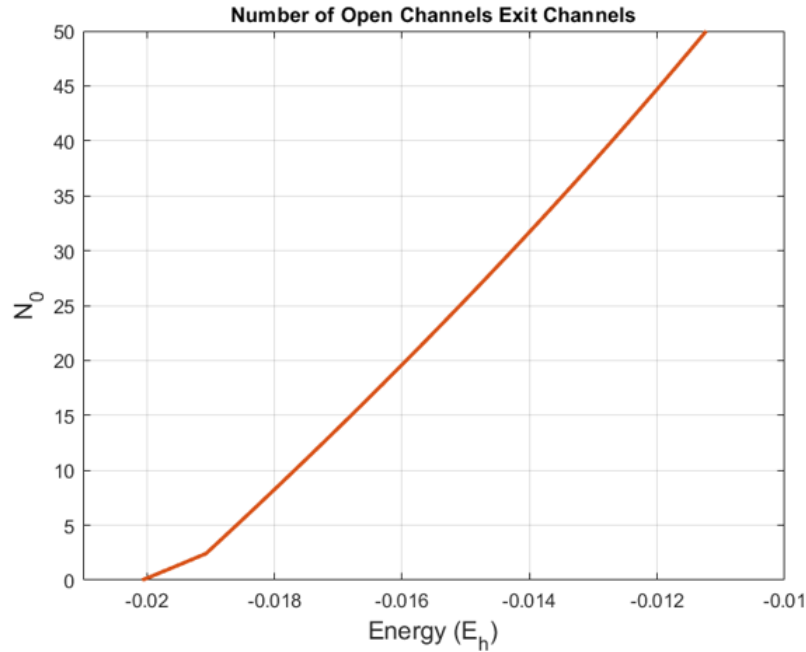

Figure 3-4: The spike at -1.90×10^{-2} corresponds to the KRb well becoming accessible.
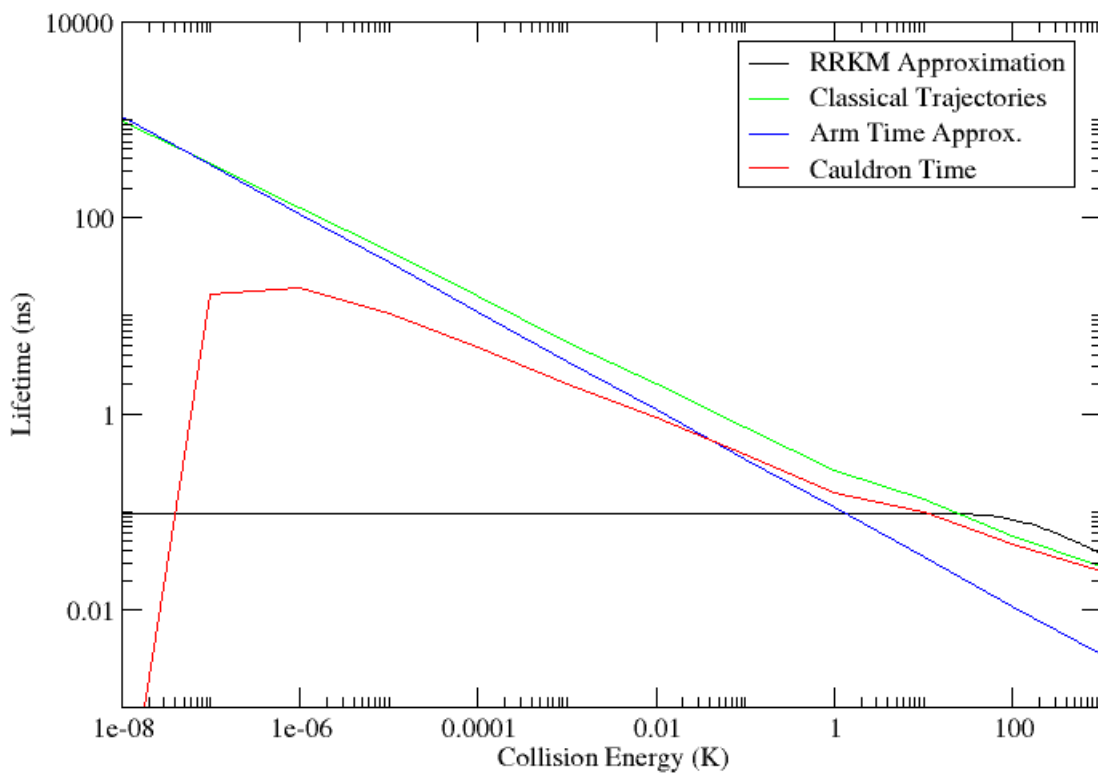
Figure 3-5: The green classical trajectory curve is calculated with one point at each order of magnitude in collision energy. Each of these points then is one trajectory which begins at $R_i = 100a_0$ at precisely the bottom of the entrance channel potential well. The system is given some amount of collision energy (as determined by the x-axis) entirely in the y_2 direction. This means there is no relative motion between the atoms in the initial KRb dimer, and the kinetic energy between this dimer and the lone K atom is shown on the x-axis. The calculations of the other curves are detailed throughout Section 3.5.

Figure 3-6: The quantum energy levels of the K_2 dimer are plotted in color, while the potential energy curve of the K_2 Morse potential is plotted in black. The values of these energy levels are given in 3.1
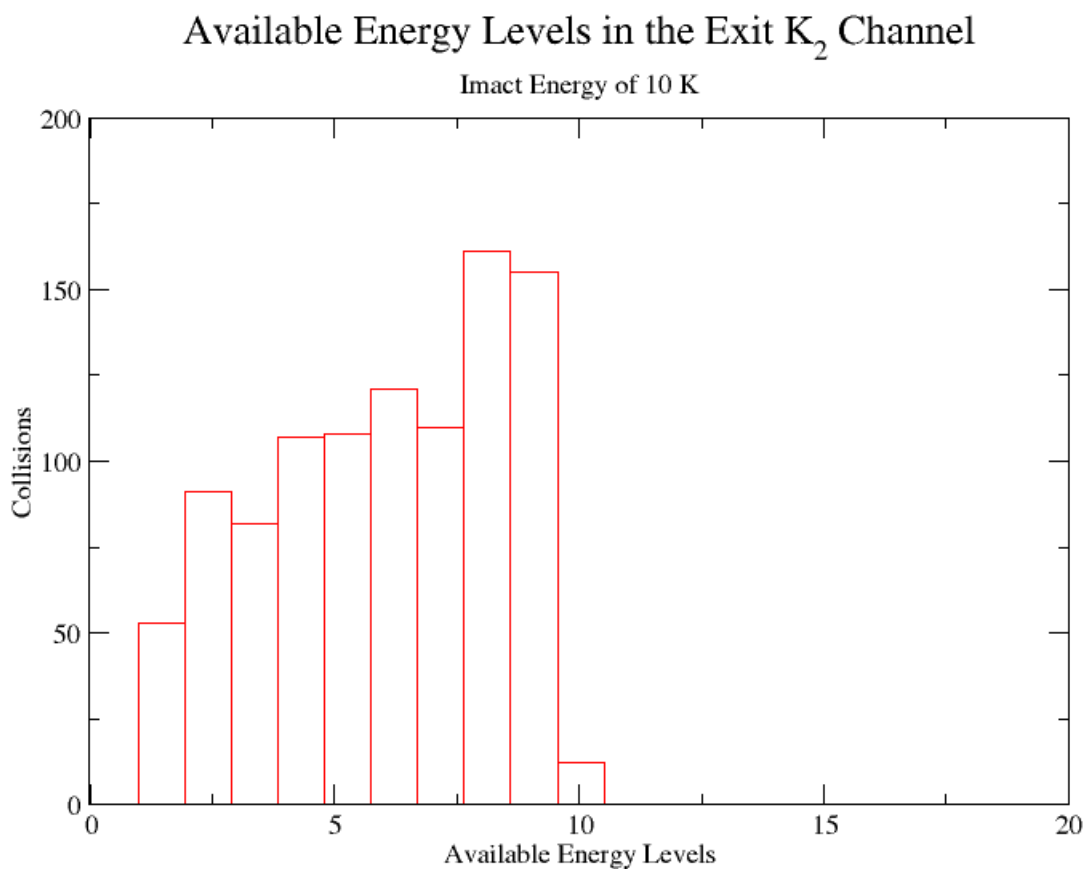
Figure 3-7: Each collision is a classically calculated trajectory with $R_i = 100a_0$, $KE = 10K\hat{y}_2$ and , $\theta_i = \theta_{\text{equilibrium}} + \epsilon$ where ϵ is some small, randomly selected deviation from the bottom of the entrance arm well. Only 20 trajectories had K_2 products with enough energy such that all 10 of the quantum energy levels were available.
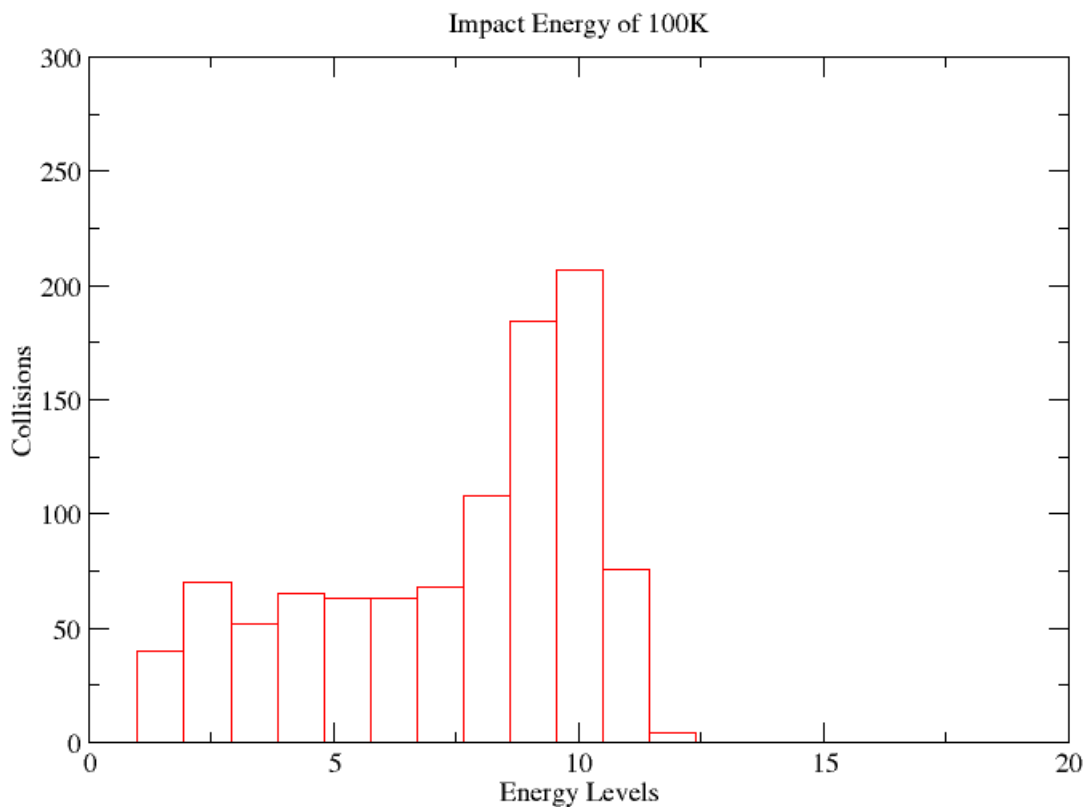
Figure 3-8: This graph was made by the same exact procedure as that described for Figure 3-7. The only difference is that the kinetic collision energy is an order of magnitude larger. Obviously, at some energy between 10 K and 100 K, the 11th and 12th quantum energy levels become accessible. Sense is made of this by considering that the energy levels are spaced by approximately 50 K near the bottom of the K_2 well.
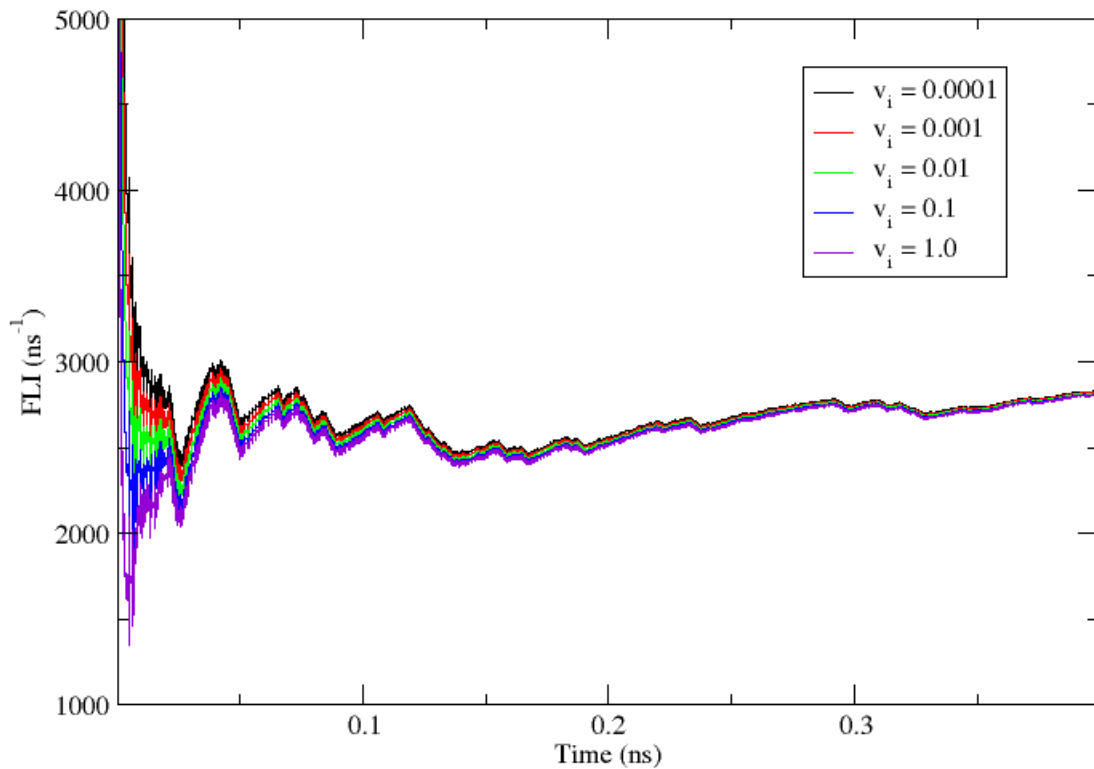
Figure 3-9: The FLI plotted for various initial deviation vector component magnitudes. The units for the initial values of the deviation vector v_i components (each of the 6 deviation vector components are equal for this plot) are Bohr radii. Despite huge variation at short times, the curves converge quickly. The fact that at large times (most K+K+Rb collisions last 0.1 ns or less) the FLI does not tend towards 0 is an indication of chaotic behavior.
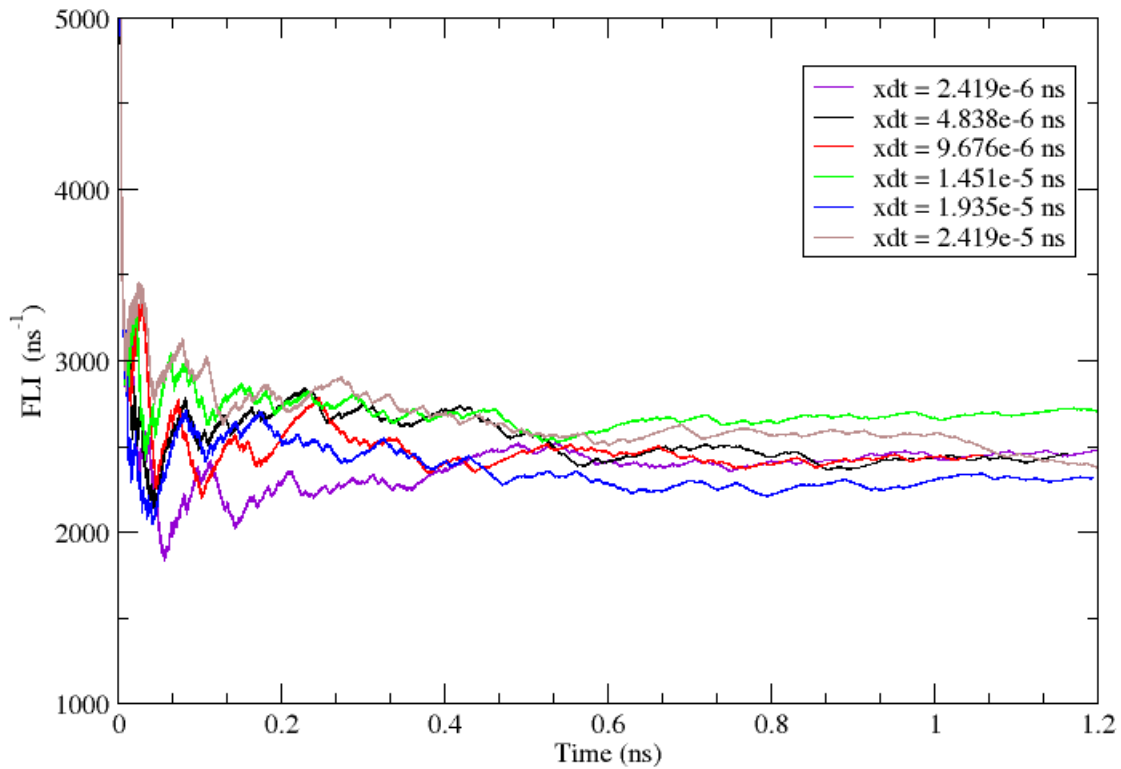
Figure 3-10: The FLI hovers near 2500 ns^{-1} in the long time limit for integrator step sizes $< 10^{-6}$ ns. The green and blue curves corresponding to time steps of 1.454×10^{-5} ns and 1.935×10^{-5} ns respectively show significant deviation from the FLIs calculated for smaller time step sizes. The brown curve corresponding to $xdt = 2.419 \times 10^{-5}$ ns happens to intersect the 3 converged curves (for small time step) at roughly the right end of this figure, but this is only a coincidence. The deviation between the brown curve and the three converged curves is more obvious in the range from $t = 0.6$ ns to $t = 1.0$ ns.
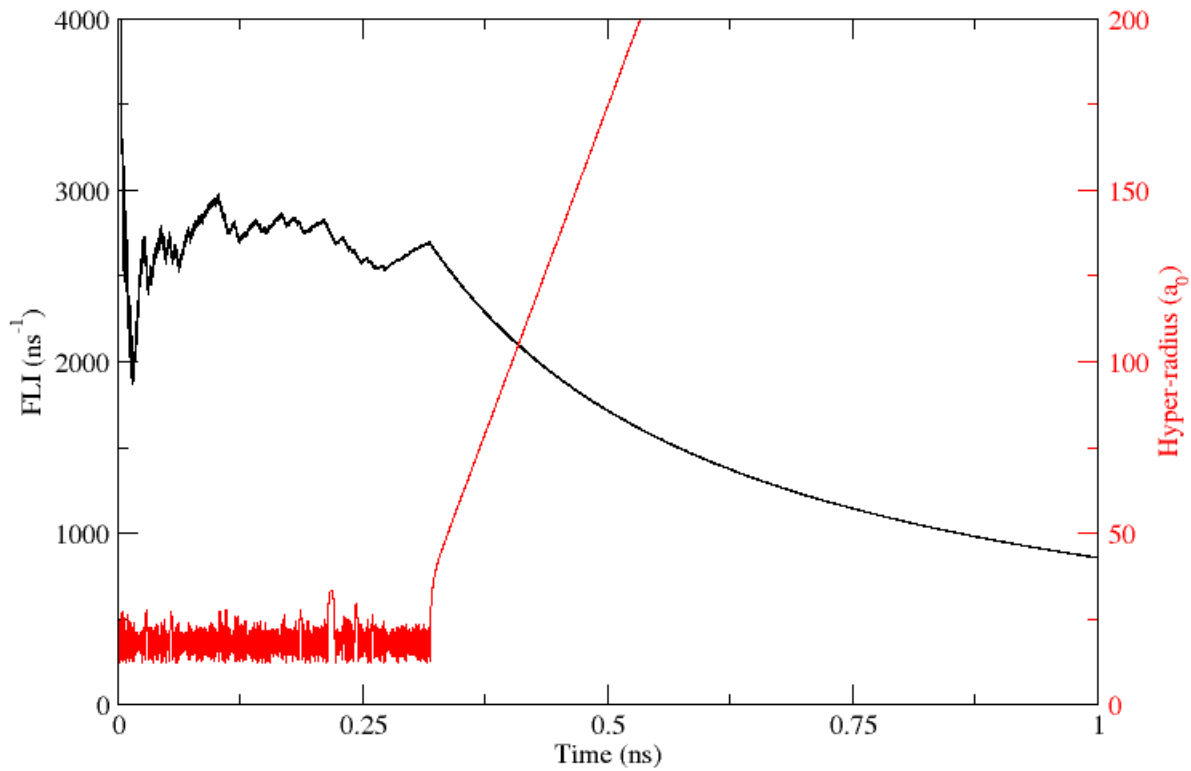
Figure 3-11: The three body collision complex undergoes hundreds of close interactions before randomly obtaining a specific distribution of energy between the degrees of freedom which allows the system to escape the cauldron. The FLI begins trending smoothly to 0 at the exact moment the complex breaks up, as expected. This clear shift in the shape of the FLI curve is a dead-giveaway that chaotic behavior gave way to regular behavior.
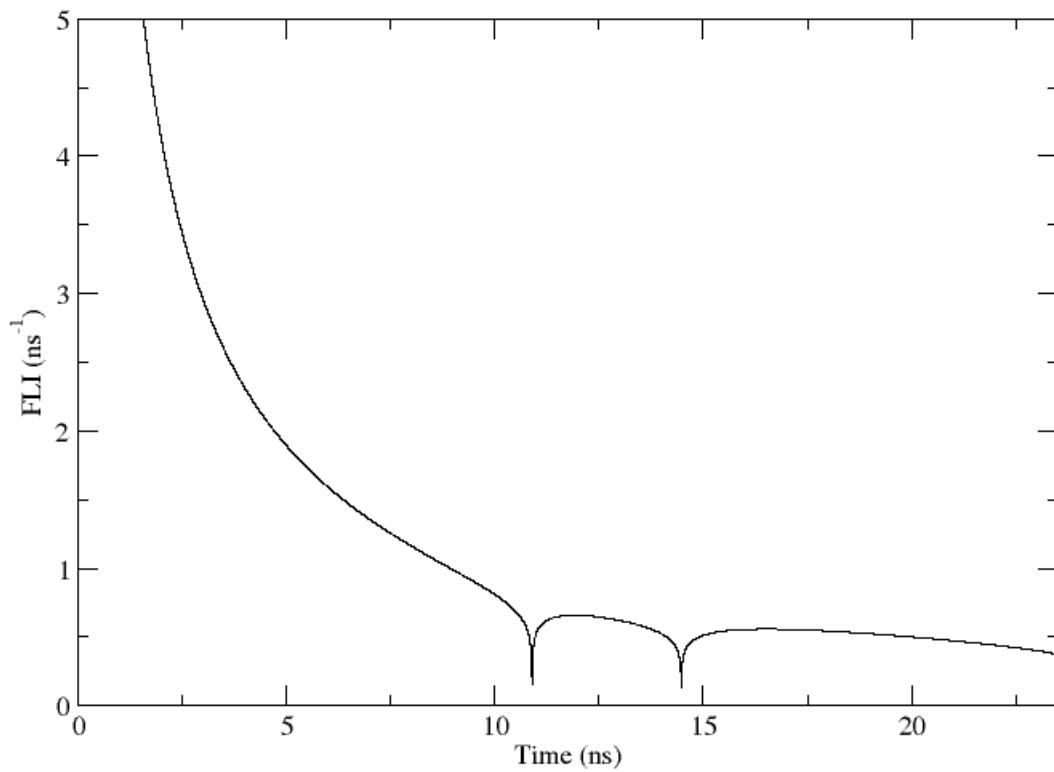
Figure 3-12: The oscillator goes through only two oscillations during the duration of this calculation (the period is roughly 12 ns) and the FLI is already very clearly trending towards 0. The two sharp declines are points where the two trajectories represented by the deviation vector get closer to each other than throughout the preceding times in the calculation.
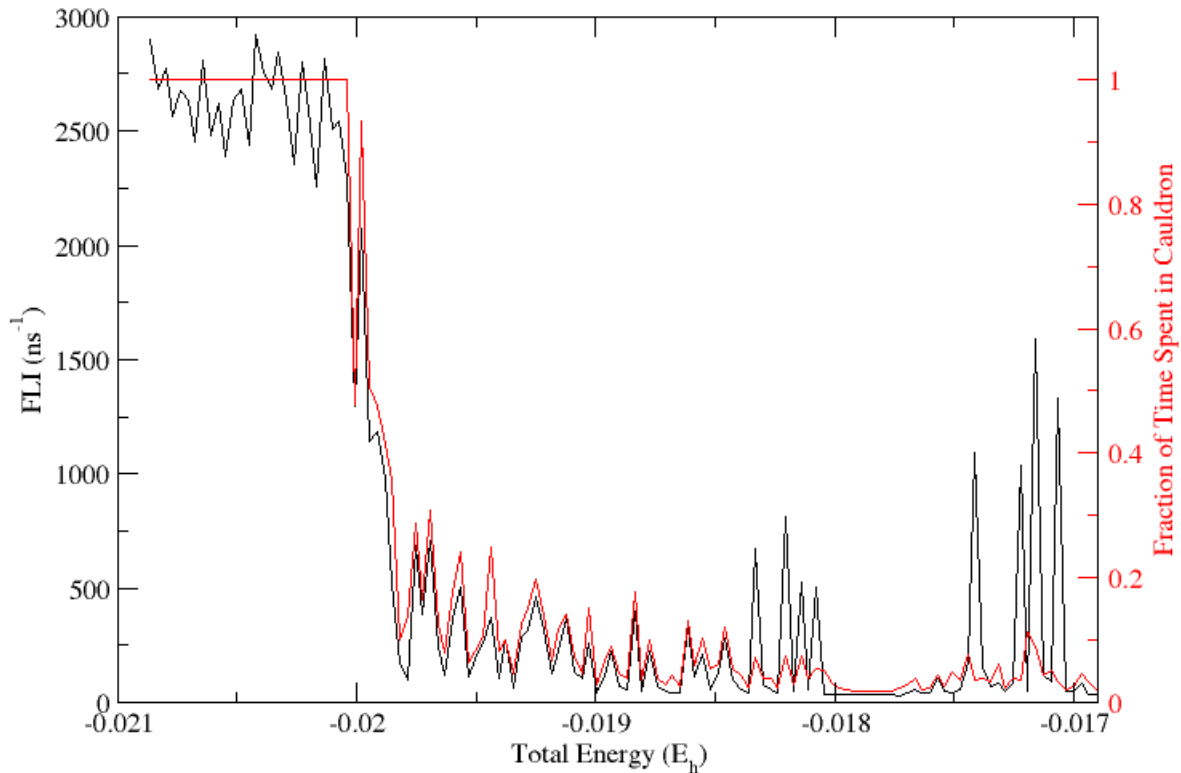
Figure 3-13: As the reader is already aware, the FLI is of course generally a function of time. However in this plot precisely one value is shown for each individual trajectory. This value is chosen to be the FLI after 1.5 ns of collision time has passed (inspecting Figure 3-10 will show that this is sufficiently long time for the FLIs to have reasonably converged, that is to within roughly 15% of their actual long time limit value). This finite FLI calculation time explains the rather noisy behavior at low total energy.

Chapter 4

Conclusions

4.1 Summary

The results of the classical calculations of the collision complex lifetimes and the semi-classical RRKM approximations certainly do not agree. At low collision energies, the classically calculated lifetimes drop below 0, of course not a physically accurate result. At higher collision energies (roughly 10 to 1000 K) the two lifetime calculation methods agree to within an order of magnitude, but this is likely coincidental. Despite the inability of this paper to demonstrate agreement between these two lifetime calculation approaches, several conclusions may still be drawn from the calculations.

For example, we found that even with an 8th order symplectic integrator running in quad precision, the most chaotic K+K+Rb collisions do not have converging trajectories. Interestingly, while the exact individual trajectories do not converge in time step, the FLI does appear to converge with respect to integrator time step size. Furthermore, the FLI is insensitive to the initial magnitude of the deviation vector on which it's definition is based. Thus the FLI is an extremely forgiving tool with which to determine if chaos is present in a system. Additionally, the FLI changes behavior quickly and noticeably if the system suddenly stops exhibiting chaos. This feature of the FLI seems to be an especially useful one that could aid in calculating more accurate collision complex lifetimes.

Additionally, we found that the vast majority of K+K+Rb collisions do not exceed a hyperradius greater than 150 a_0 without exiting the cauldron and continuing on to infinite hyperradius. However, as previously described this fact does not turn out to be especially useful in defining a boundary between the collision complex and the exit arms. Due to the slow, integrable behavior of the system in the exit arms, the collision complex lifetime is effectively watered down with uninteresting time spent slowly oscillating out of the complex to infinite hyperradius. Thus, choosing one hyperradius to distinguish between the collision complex and the arms will necessarily inflate the collision complex lifetimes (at least for those systems which are not prematurely terminated by reaching the cut-off hyperradius before they were finished colliding).

4.2 Future Work

Moving forward, the reason for the discrepancy in RRKM collision complex lifetime approximations and classically calculated ones could be addressed by the methods described in Section 3.5. This would serve to validate the applicability of the successful RRKM theory as well as provide a connection between semi-classical and classical calculations. The most promising method which could lead to agreement between the two lifetime calculation methods is defining the end of the collision complex as the moment where the FLI transitions behaviors. When the FLI spontaneously shifts from hovering near some positive, finite value, to falling smoothly to 0, it can be stated with certainty that the system has finished colliding and is now on its way out to infinite hyperradius.

However, the aforementioned method corrects for only the arm-time spent after the collision has ended, not the entrance arm-time. That is, the collision complex lifetimes were calculated with systems that began far out in the KRb entrance channel and slowly made their way into the 3-body cauldron. Instead, future work could start the system inside the cauldron at $t = 0$ and add some kinetic energy that would have been gained by the system as it fell out of the 2-body KRb channel and into the much deeper 3-body well.

Additionally, future work may seek to find some way to correct for the failure of the trajectories to converge in integrator step size. Perhaps an average could be taken for each trajectory integrated with numerous different step sizes. However, care would need to be taken to ensure that this average has physical meaning. An alternative method would be to average lifetimes calculated using only one step size but with some tiny deviations in the initial conditions. We expect that these two methods would lead to the same average since changing the integrator step size effectively leads to a small "deviation in initial conditions" at some time after the simulation is begun. That is, we expect that one trajectory with some set of initial conditions that is integrated with a specific step size has an identical trajectory with some very slightly different set of initial conditions that is integrated with a different step size.

Furthermore, future work may be able to make meaning of the specific value of the FLI, as opposed to only inspecting the behavior of the FLI as a function of time or the relative sizes of different FLIs. These are the only two ways that this work uses the FLI, and it is possible that there is more meaning to be garnered from this tool. Why many purely chaotic trajectories have FLI values that hover near 2700 ns^{-1} is a question that this work is unable to answer. Finally, a push to generalize this work to 3-dimensions or 4 bodies could offer more insight into the nature of these reactions.

Chapter 5

Appendix

5.1 Code

All of the code used for this work can be found on the Mehta Theory Group github at https://github.com/mehta-group-at-trinity-university/. Specifically, the program used to simulate the K+K+Rb as well as the corresponding FLI curves is entitled "adlzapp.f90" and can be found at https://github.com/marklide/Nbody.

5.2 Unit Conversions

1 au = 2.418 884 326 585 7(47) × 10^{-17} s (NIST 2018a)

1 E_h = 3.157 750 248 0407(61) × 10^5 K (NIST 2018a)

1 E_h = 2.194 746 313 6320(43) × 10^7 m^{-1} (NIST 2018a)

1 a_0 = 5.291 772 109 03(80) × 10^{-11} m (NIST 2018a)

1 a_0 = 0.529 177 249 Å(NIST 2018a)

1 atomic unit of mass = 1 m_e = 9.109 383 7015(28) × 10^{-31} kg (NIST 2018a)

1 atomic unit of action = 1 $\hbar$ = 1.054 571 817 × 10^{-34} J·s (NIST 2018a)

5.3 Deviation Vector Example

The purpose of this example is to illuminate the meaning of Equation 2.20, rewritten below for clarity.

$$\dot{\vec{v}} = \boldsymbol{J} \frac{\partial^2 \boldsymbol{H}}{\partial \vec{\gamma}^2} \vec{v}. \tag{5.1}$$

In this example we will obtain equations of motion for the deviation vector $\vec{v}$ for a 1D classical harmonic oscillator without damping via two different methods. The first method goes as follows. Using the dimensionless variables x and p for the harmonic oscillator, I define

$$p_0 = m\omega x_0, \ E_0 = m\omega^2 x_0^2, \ t_0 = \omega^{-1}. \tag{5.2}$$

Now the Hamiltonian becomes

$$H = \frac{1}{2}p^2 + \frac{1}{2}x^2. \tag{5.3}$$

The equations of motion therefore are

$$\dot{p} = \frac{-\partial H}{\partial x} = -x, \ \dot{x} = \frac{\partial H}{\partial p} = p. \tag{5.4}$$

Differentiating both of these equations with respect to time yields

$$\ddot{p} = -\dot{x} = -p, \ \ddot{x} = \dot{p} = -x. \tag{5.5}$$

The solutions to which are

$$x = c_1 \cos t + c_2 \sin t, \ p = -c_1 \sin t + c_2 \cos t. \tag{5.6}$$

By taking the difference between two sets of these equations (the second set with some other coefficients) the separation vector $\vec{v}(t)$, with initial value $\vec{v}_0$ is

$$v_x(t) = A \cos t + B \sin t, \ v_p(t) = B \cos t - A \sin t \tag{5.7}$$

is obtained. Applying initial conditions yields the full separation vector

$$\vec{v}(t) = \begin{pmatrix} v_x(t) \\ v_p(t) \end{pmatrix} = \begin{pmatrix} v_{x0} \cos t + v_{p0} \sin t \\ v_{p0} \cos t - v_{x0} \sin t \end{pmatrix}. \tag{5.8}$$

Or, written more compactly

$$\vec{v}(t) = \begin{pmatrix} \cos t + \sin t \\ \cos t - \sin t \end{pmatrix} \vec{v}_0. \tag{5.9}$$

Now I will use Equation 2.20 (same as Eqn 4.1) to prove the same result and thus demonstrate the validity and applicability of this equation. The first derivative of the a general Hamiltonian with respect to a (in this case one dimensional) phase space vector $\vec{\gamma}(t) = \begin{pmatrix} x(t) \\ p(t) \end{pmatrix}$ is given by

$$\overrightarrow{\left(\frac{\partial H}{\partial \vec{\gamma}} \right)} = \begin{pmatrix} \frac{\partial H}{\partial x} \\ \frac{\partial H}{\partial p} \end{pmatrix} = \begin{pmatrix} \frac{\partial V}{\partial x} \\ \frac{p}{m} \end{pmatrix} \tag{5.10}$$

where V is the potential and m is the mass. Thus, the second derivative of the Hamiltonian with respect to $\vec{\gamma}$ is

$$\frac{\partial^2 H}{\partial \vec{\gamma}^2} = \begin{pmatrix} \frac{\partial^2 H}{\partial x^2} & \frac{\partial^2 H}{\partial x \partial p} \\ \frac{\partial^2 H}{\partial x \partial p} & \frac{\partial^2 H}{\partial p^2} \end{pmatrix} = \begin{pmatrix} \frac{\partial^2 V}{\partial x^2} & 0 \\ 0 & \frac{1}{m} \end{pmatrix}. \tag{5.11}$$

Using our dimensionless Hamiltonian given by Eqn. 4.3 Eqn. 4.1 becomes

$$\dot{\vec{v}}(t) = \begin{pmatrix} 0 & 1 \\ -1 & 0 \end{pmatrix} \begin{pmatrix} 1 & 0 \\ 0 & 1 \end{pmatrix} \vec{v}(t). \tag{5.12}$$

Multiplying out these matrices and splitting the deviation vector into its components yields

$$\begin{pmatrix} \dot{v}_x(t) \\ \dot{v}_p(t) \end{pmatrix} = \begin{pmatrix} -v_p(t) \\ v_x(t) \end{pmatrix}. \tag{5.13}$$

Differentiating both sides with respect to time leaves us with

$$\begin{pmatrix} \ddot{v}_x(t) \\ \ddot{v}_p(t) \end{pmatrix} = \begin{pmatrix} -\dot{v}_p(t) \\ \dot{v}_x(t) \end{pmatrix} = \begin{pmatrix} -v_x(t) \\ -v_p(t) \end{pmatrix}. \tag{5.14}$$

The solutions to which are

$$v_x(t) = c_1 \cos t + c_2 \sin t, \quad v_p(t) = -c_1 \sin t + c_2 \cos t. \tag{5.15}$$

Finally, applying the initial conditions $\vec{v}(0) = \vec{v}_0$ yields the exact same result as before

$$\vec{v}(t) = \begin{pmatrix} \cos t + \sin t \\ \cos t - \sin t \end{pmatrix} \vec{v}_0. \tag{5.16}$$

For problems as simple as this, the added mental complexity of using Eqn 4.1 (which contains unwieldy an derivative with respect to a vector) is certainly not worth it. However when analytical solutions to the trajectories are not available (as is the case for the harmonic oscillator) Eqn. 4.1 allows us to integrate the deviation through time, simultaneously calculating the original trajectory at each time step.

Bibliography

M. H. Anderson, J. R. Ensher, M. R. Matthews, C. E. Wieman, and E. A. Cornell. Observation of bose-einstein condensation in a dilute atomic vapor. *Science*, 269(5221):198–201, 1995. ISSN 0036-8075. doi: 10.1126/science.269.5221.198. URL https://science.sciencemag.org/content/269/5221/198.

M. T. Bell and T. P. Softley. Ultracold molecules and ultracold chemistry. *Molecular Physics*, 107(2): 99–132, 2009. doi: 10.1080/00268970902724955. URL https://doi.org/10.1080/00268970902724955.

J. N. Byrd, J. A. Montgomery, and R. Côté. Structure and thermochemistry of k_2rb, krb_2, and k_2rb_2. *Phys. Rev. A*, 82:010502, Jul 2010. doi: 10.1103/PhysRevA.82.010502. URL https://link.aps.org/doi/10.1103/PhysRevA.82.010502.

A. Christianen, T. Karman, and G. C. Groenenboom. Quasiclassical method for calculating the density of states of ultracold collision complexes. *Phys. Rev. A*, 100:032708, Sep 2019. doi: 10.1103/PhysRevA.100.032708. URL https://link.aps.org/doi/10.1103/PhysRevA.100.032708.

P. Cornille. *Advanced Electromagnetism and Vacuum Physics*. World Scientific, 2003.

J. F. E. Croft and J. L. Bohn. Long-lived complexes and chaos in ultracold molecular collisions. *Phys. Rev. A*, 89:012714, Jan 2014. doi: 10.1103/PhysRevA.89.012714. URL https://link.aps.org/doi/10.1103/PhysRevA.89.012714.

C. Froescilé, E. Lega, and R. GONCZI. Fast lyapunov indicators. application to asteroidal motion. *Celestial Mechanics and Dynamical Astronomy*, 67:41–62, 01 1997. doi: 10.1023/A:1008276418601.

I. Gel'fand and N. Vilenkin. *Generalized Functions: Applications of Harmonic Analysis*. Generalized functions. Elsevier Science, 2014. ISBN 9781483262246. URL https://books.google.com/books?id=nAnjBQAAQBAJ.

E. Grumbling and M. Horowitz. *Quantum Computing: Progress and Prospects*. The National Academies Press, Washington, DC, 2019. ISBN 978-0-309-47969-1. doi: 10.17226/25196. URL https://www.nap.edu/catalog/25196/quantum-computing-progress-and-prospects.

R. D. Levine. *Molecular Reaction Dynamics*. Cambridge University Press, 2005. doi: 10.1017/CBO9780511614125.

A.-S. Libert, C. Hubaux, and T. Carletti. The Global Symplectic Integrator: an efficient tool for stability studies of dynamical systems. Application to the Kozai resonance in the restricted three-body problem.

Monthly Notices of the Royal Astronomical Society, 414(1):659–667, 06 2011. ISSN 0035-8711. doi: 10.1111/j.1365-2966.2011.18431.x. URL https://doi.org/10.1111/j.1365-2966.2011.18431.x.

H.-D. Meyer. Theory of the liapunov exponents of hamiltonian systems and a numerical study on the transition from regular to irregular classical motion. *The Journal of Chemical Physics*, 84:3147–3161, 1986. doi: 10.1063/1.450296. URL https://aip.scitation.org/doi/10.1063/1.450296.

P. M. Morse. Diatomic molecules according to the wave mechanics. ii. vibrational levels. *Phys. Rev.*, 34: 57–64, Jul 1929. doi: 10.1103/PhysRev.34.57. URL https://link.aps.org/doi/10.1103/PhysRev.34.57.

NIST. Searchable bibliography on the constants, 2018a. URL https://physics.nist.gov/cuu/Constants/bibliography.html.

NIST. Dipotassium, 2018b. URL https://webbook.nist.gov/cgi/inchi?ID=C25681805&Mask=1000#Diatomic.

NIST. Potassium, compound with rubidium (1:1), 2018c. URL https://webbook.nist.gov/cgi/cbook.cgi?ID=C12333390&Units=SI&Mask=1000#Diatomic.

N. W. M. Ritchie, E. R. I. Abraham, Y. Y. Xiao, C. C. Bradley, R. G. Hulet, and P. S. Julienne. Trap-loss collisions of ultracold lithium atoms. *Phys. Rev. A*, 51:R890–R893, Feb 1995. doi: 10.1103/PhysRevA. 51.R890. URL https://link.aps.org/doi/10.1103/PhysRevA.51.R890.

C. Schlier and A. Seiter. High-order symplectic integration: an assessment. *Computer Physics Communications*, 130(1):176–189, 2000. ISSN 0010-4655. doi: https://doi.org/10.1016/S0010-4655(00)00011-4. URL https://www.sciencedirect.com/science/article/pii/S0010465500000114.

R. D. Vogelaere. Methods of integration which preserve the contact transformation property of the hamilton equations. Mar 1956. URL https://curate.nd.edu/show/6395w665s0q.